X-ray analysis of protective coatings

Zoestbergen, Edzo

3 Microstructure and morphology of magnetron sputtered coatings

In general the microstructure and the state of stress of a coating have a considerable influence on its performance in practical use. Consequently, in many cases it is important to control accurately the crystallographic orientation, surface texture and residual stresses. Knowing the physical phenomena that control the specific properties of the deposit makes it possible to choose the right deposition conditions. However, to be able to comprehend the physical processes it is, first of all, necessary to vary the deposition parameters and study the deposits obtained [1].

In this chapter, the different magnetron sputtered TiN coatings are characterised. The influence of the deposition parameters on the microstructure, section 3.1, and the residual stresses, section 3.2 and 3.3, of the coatings are determined and the mutual relationship is assessed.

3.1 Microstructure and texture

In this section, the surface texture and crystallographic orientation of the magnetron sputtered specimens are investigated using SEM and X-ray diffraction technique. Further, the influence of the deposition parameters on the thickness of the coatings is examined.

3.1.1 Layer thickness

The so-called hole drilling method was applied by Tan [2] to determine the thickness of the coatings. A hole is drilled through the coating with a ball of a known radius. Comparing the radius of the circle of the drilled hole at the surface of the coating and at the interface makes it possible to calculate the thickness of the coating. These results are verified by preparing cross sections and measuring the layer thickness in an SEM. The results are listed in Table 3.1.

It can be concluded that for batches 1 and 3, where the Ti concentration was the variable, the actual layer is getting thinner upon decreasing titanium concentration, i.e. upon adding more nitrogen. This is because the titanium target gets ‘poisoned’ with adsorbed nitrogen atoms. The sputter rate of Ti drops because the ion bombardment sputters now both kinds of atoms, Ti as well as the adsorbed nitrogen. Consequently, the coating will be thinner with decreasing Ti concentration [3]. The specimens from the second batch show the

expected behaviour; i.e. the thickness of the deposit is linear proportional to the deposition time.

A comparison of the absolute values of the different bias voltages indicates that the layer thickness decreases with an increasing bias voltage. All the specimens from the –40V batch have a thickness equal or thicker than the specimens from the –80V batch. Only the specimen with a deposition time of 60 minutes from the second batch, -65V, is an exception. The decrease in thickness with increasing bias voltage is probably due to the higher (re)-sputter rate for the specimens prepared at a higher bias voltage. However, one should realise that the degradation of the target during previous experiments might also have an influence on the absolute thickness of the coatings. This may also be the reason for the deviation of the film thickness of the 60 minutes specimen from the second batch.

Table 3.1 Influence of the deposition parameters on the coating thickness

		Coating thickness [µm]								
Ti concentration [%]		40	50	55	55	55	55	60	70	80
Deposition time [min]		60	60	30	45	60	90	60	60	60
Bias voltage [V]	-40	1.9	3.0			3.1		3.2	4.0	4.2
	-65			2.0	3.0	4.0	6.2			
	-80	1.9	2.4			2.4		2.5	3.0	3.3

3.1.2 Microstructure and morphology

The specimens from the first and third batch were investigated using a scanning electron microscope. Top view micrographs were taken of the entire series and cross sectional micrographs were only taken of a number of specimens.

Top view micrographs of the specimens from the –40 V series, Figure 3.1, show that the specimens prepared at a Ti concentration of 40 and 80% are clearly different from the other four specimens which show a distinct resemblance. These four specimens have a surface that appears to be rather rough and the grains have an elongated morphology. The surface does not look very dense. The elongated morphology is probably due to the deposition geometry and is also visible in the micrographs of the specimens from the third batch. The two other specimens have a surface that looks rather flat and appears to be dense with a much finer grain structure. The elongated morphology is not present. The difference between the two specimens is the roughness of the film surface. The 80% titanium specimen has a rougher surface.

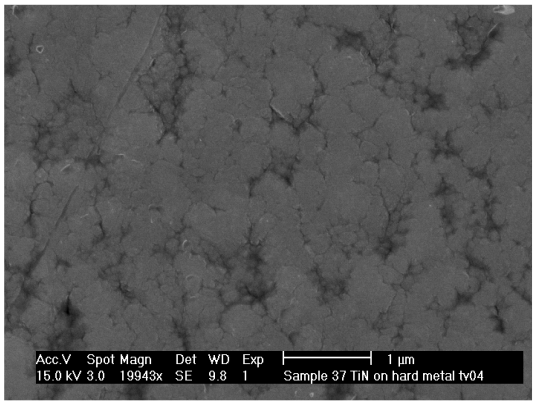

(a) 40% Ti

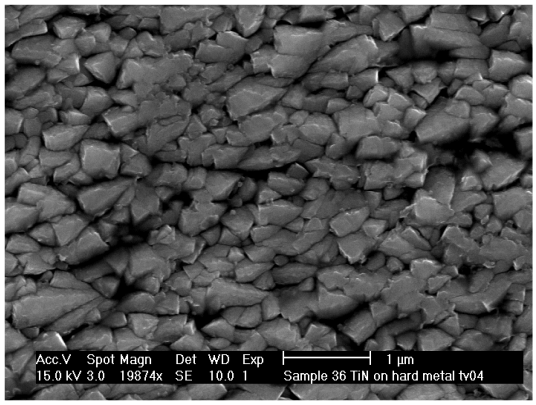

(b) 50% Ti

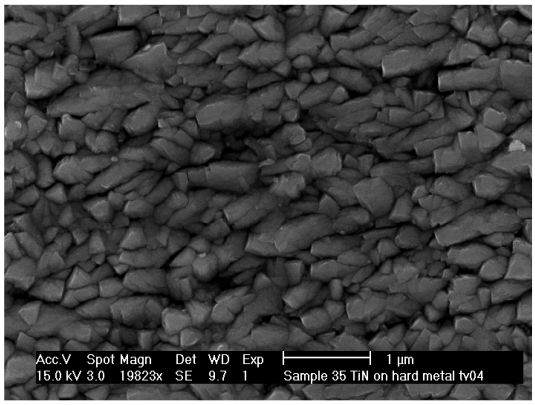

(c) 55% Ti

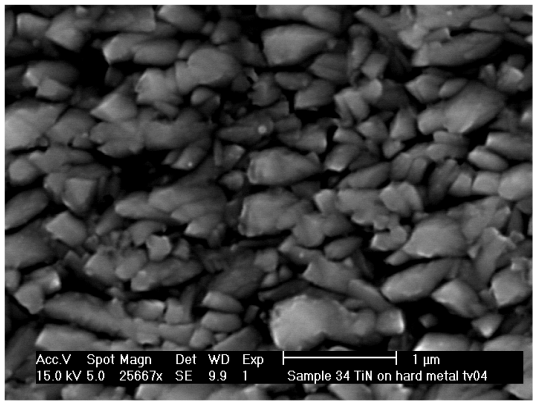

(d) 60% Ti

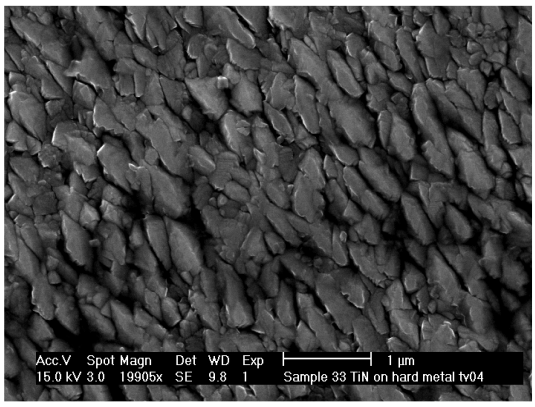

(e) 70% Ti

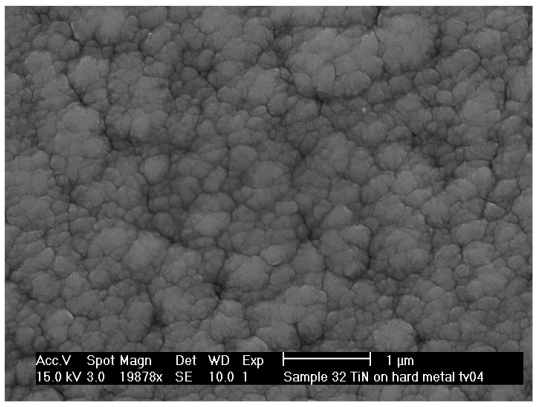

(f) 80% Ti

Figure 3.1 Top view micrographs of the specimens from the first batch, bias voltage -40V. The specimens prepared at a titanium concentration of 40 and 80% show a distinct difference from the other specimens.

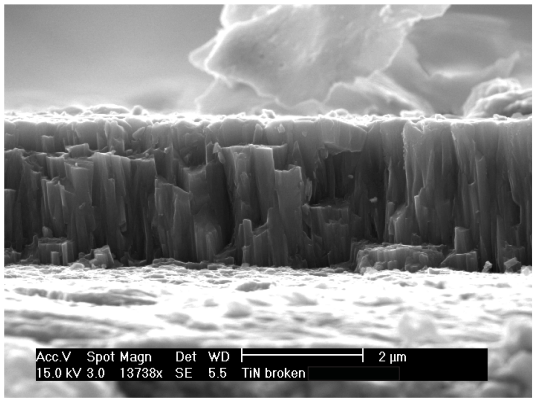

(a) 50% Ti

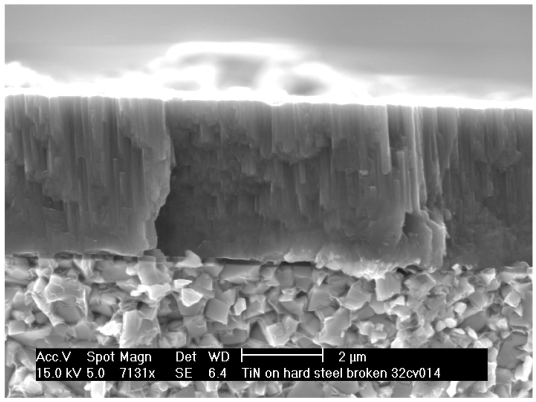

(b) 80% Ti

Figure 3.2 Cross sections of two specimens from the first batch prepared at 50 and 80% titanium, respectively (a) and (b). There is a difference visible between the columnar structures of both the specimens.

The cross sectional micrographs of fractured specimens in Figure 3.2 are obtained by cooling the coated substrates to liquid nitrogen and fracture them when the temperature is below the ductile-to-brittle transition temperature. Both the specimens have a columnar structure but for the specimen prepared at 80% Ti the columns are rather straight. The columns in the other specimen have a tapered form and the width of the columns is larger than for the 80% specimen. The specimens prepared at a Ti concentration of 55, 60 and 70% have the same morphology as the 50% specimen and the 40% specimen has again a larger resemblance with the 80% one. The intermediate layer visible in both micrographs of Figure 3.2 is a pure Ti layer which is grown to assure a good bonding between the coating and the substrate (Good visible in Figure 3.5.)

An SEM investigation of the specimens of the –80V series, Figure 3.3, indicates that the difference between the surface structure of the specimens is not very big. They all seem to have a smooth dense surface structure, one slightly denser than the other, and they all have a morphology, which is elongated. The cross sectional micrograph, Figure 3.4-(a), shows a columnar structure and this is found in all the specimens from this batch. Only the specimen prepared at 80% Ti has a structure that looks finer and the columns are not clearly visible.

Discussion

The microstructure of the deposits is fully determined by the deposition parameters. In order to draw conclusions concerning the deposits it is essential to define the precisely the processes that take place during the deposition.

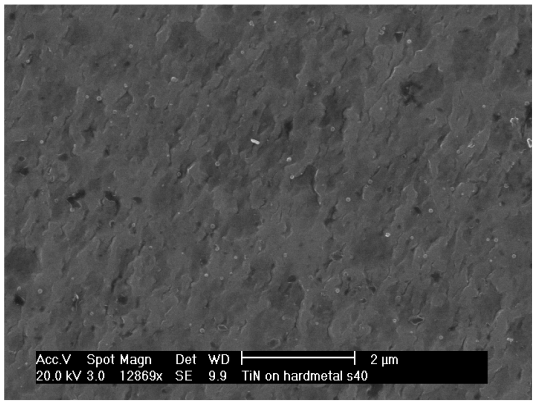

(a) 40% Ti

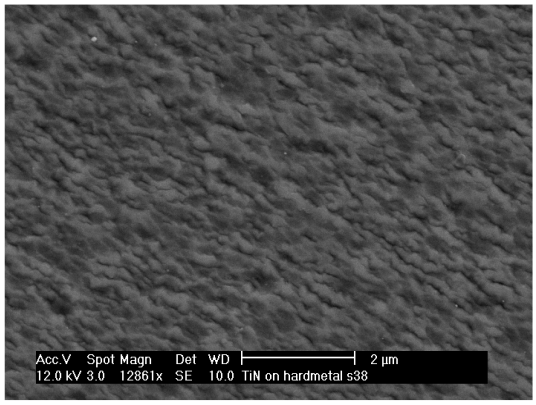

(b) 50% Ti

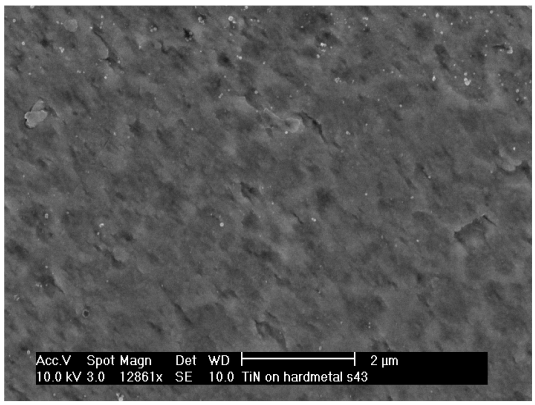

(c) 55% Ti

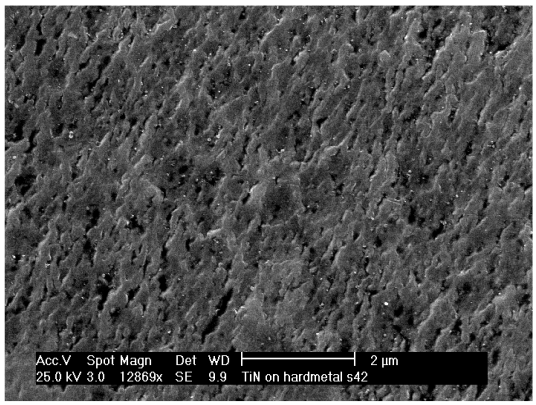

(d) 60% Ti

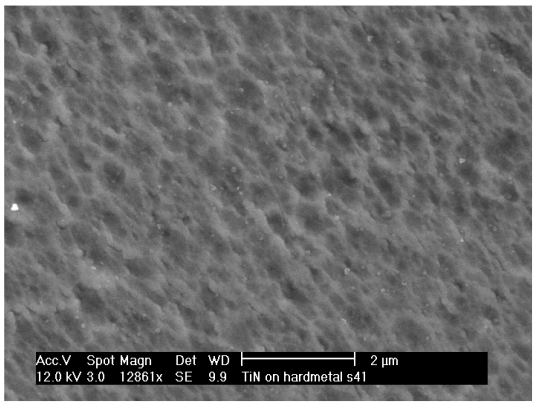

(e) 70% Ti

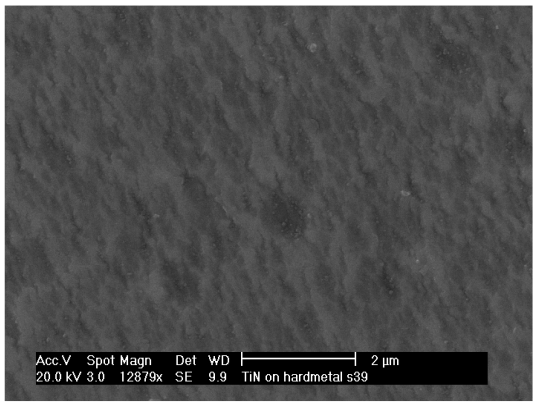

(f) 80% Ti

Figure 3.3 Specimens from the third batch, bias voltage of -80V. There is no large difference visible between the specimens within this batch. The directional structure is probably a consequence of the bombardement during deposition.

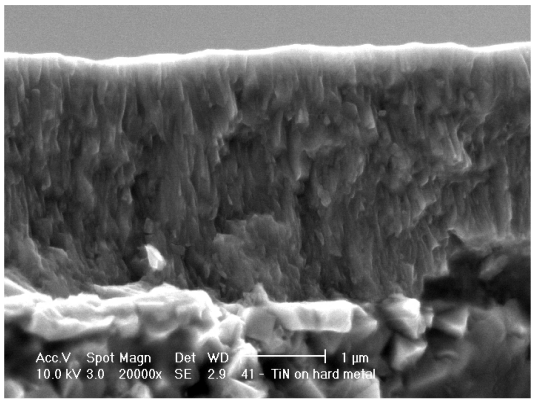

(a) 60% Ti

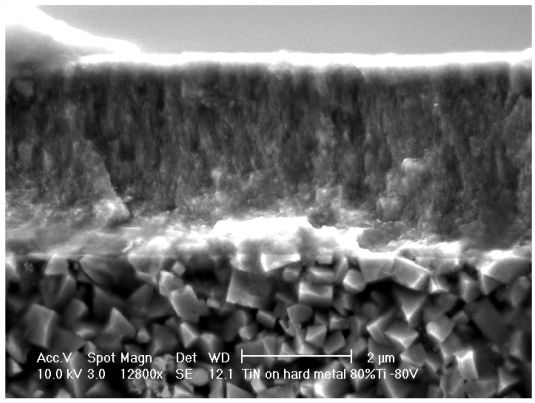

(b) 80% Ti

Figure 3.4 Cross sections of two specimens from the third batch prepared at 60 and 80% titanium. The columnar structure is present in the 60% but is not so clearly visible in the 80% specimen.

The coating-atom condensation process for pure metals is usually divided in three stages [4]. The first stage is the collision of incident atoms with the surface. They transfer kinetic energy to the lattice and become loosely bonded "adatoms'. These adatoms may diffuse over the surface, exchanging energy with the lattice and other adsorbed species (stage two). The diffusion of these adatoms ends when they are desorbed, by evaporation or sputtering, or become trapped at low energy sites. The final stage is the readjustment of the trapped atoms within the lattice. During the three stages different physical processes are involved in the trajectory of an atom:

- Shadowing, the geometric interaction between the roughness of the growing surface and the angular direction of the arriving atoms.
- The surface diffusion, which is related to the activation energy for surface diffusion.
- Bulk diffusion, which depends on the activation energy for bulk diffusion.
- And the desorption which is controlled by the sublimation energy.

At different temperature ranges different processes might dominate. Therefore, the zone model for growth is divided into ranges determined by the ratio between the deposition and the melting temperature, i.e. $T_{\text{deposition}}$ over T_{melt}. The existing models are roughly divided in three zones.

1. $T_{\text{deposition}}/T_{\text{melt}}<0.3$ consists of tapered crystals with domed tops, which are separated by porous boundaries: low activity of surface diffusion.
2. $0.3<T_{\text{deposition}}/T_{\text{melt}}<0.5$ consists of columnar grains separated by distinct dense, intercrystalline boundaries. The surface has a smooth appearance.
3. $T_{\text{deposition}}/T_{\text{melt}}>0.5$ consists of equiaxed grains completely controlled by bulk diffusion.

(The influence of the bias voltage is not considered and for a reactive sputtered film also the heat of formation can be of importance in the deposition process.)

TiN has a melting temperature of 3203 K and the deposition temperature is only 620 K. Therefore, the TiN layers should have a morphology that is comparable to that of the first zone. Indeed the bulk of the specimens from the first batch has a structure consisting of tapered crystals with domed tops. The nodular flaw, Figure 3.5, found in the specimen prepared at 70% also points towards a zone 1 driven growth. Nodular flaws of the same kind are also found in zone 1 sputtered chromium coatings [4]. Besides the temperature there are two other process parameters varied and the questions that have to be answered are:

- What is the influence of the Ti concentration?
- And what is the influence of the bias voltage on the morphology and microstructure of the coating?

The Ti concentration and the bias voltage have both an influence on the ratio of the fluxes of ions and atoms, J_{ions}/J_{atoms}, which impinge on the surface. By increasing the bias voltage, the amount of ions impinging on the surface will increase. A result of this is that badly adherent particles will be removed. This is comparable with an increase in surface diffusivity, a change to zone 2, which will also result in fewer faults as well as fewer badly adhered particles. This change in zone due to ion bombardment is also found in literature [3]. The zone 2 deposits have columnar grains and this is the case for the specimens from the third batch, Figure 3.4. The columnar structure is a result of a $T_{deposition}/T_{melt}$ sufficient to reduce the adatoms surface density so there are no new nucleation sites and the existing crystallites grow as columns by a localised epitaxial process. It is also believed that the change in structure of the first and last specimen from batch 1 is a consequence of a change in ratio of flux of ions and atoms. This becomes clear after the calculation of the macro residual stresses in section 3.2. Small differences within both batches are difficult to explain but

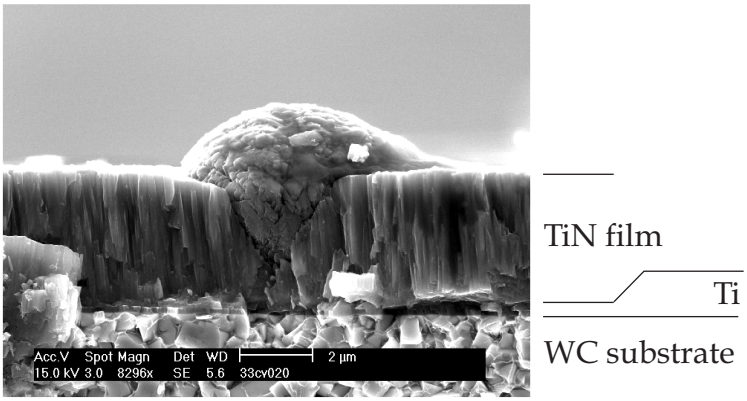

Figure 3.5 Nodular grow flaws are only seen in specimens with a low internal stress.

may be generated by a difference in chemical compositions of the coatings.

3.1.3 Crystallographic orientation

The crystallographic orientation of the grains in the specimens is determined with a XRD ψ-goniometer. The intensity of a specific diffraction peak is measured as a function of the polar and azimuth angles ψ and φ, Figure 2.6. The measured intensity is a direct indication of the grain alignment, although sometimes it is necessary to perform the measurements on different reflections to get a clear picture of the crystallographic orientation. The results presented in this section can only be used qualitatively because no background, defocus* or layer thickness correction are carried out on the acquired data. For the texture measurements, the {200} and the {220} reflections are used.

Figure 3.6 shows the pole figures of the {200} and the {220} reflections of the specimen deposited at a bias voltage of –65V during 60 minutes. The {200} reflections have a maximum at ψ=45° and this maximum is found in a small φ region. This is called a *biaxial texture*; i.e. a texture with a preference for the plane that grows parallel to the interface and a preferential growth direction within this plane.

A texture is normally defined by the plane that lies parallel to the specimen surface and a direction in the plane of the specimen surface. The planes that grow parallel to the interface for the specimen from Figure 3.6 are the {220} planes because the {220} reflections have a maximum intensity in the middle. The direction in the plane of the specimen is usually called the rolling direction because the first textures were discovered in rolled material. The rolling direction provides an unambiguous direction in the plane of the specimen. The same analogy will be used here although in the magnetron sputtered specimens there is no rolling direction. The rolling direction for the biaxial textured specimens is defined as the direction in which the {200} reflections have a maximum in intensity, φ=45 and φ=225 degrees. The direction parallel to the rolling direction is then the [2$\underline{2}$0] direction and the crystallographic orientation is defined by (220)[2$\underline{2}$0]. All the specimens from the second batch and the first five specimens from the first batch, that is from 40 to 70% Ti concentration, have a (220)[2$\underline{2}$0] crystallographic orientation. There is only one major difference between these specimens, i.e. the exact intensity distribution is not the same for the different specimens, which is due to layer thickness and the texture development within the coatings.

* During the ψrotation, part of the specimen is moved in front and a part is moved behind the defocusing circle of the diffractometer, which will influence the measured intensity.

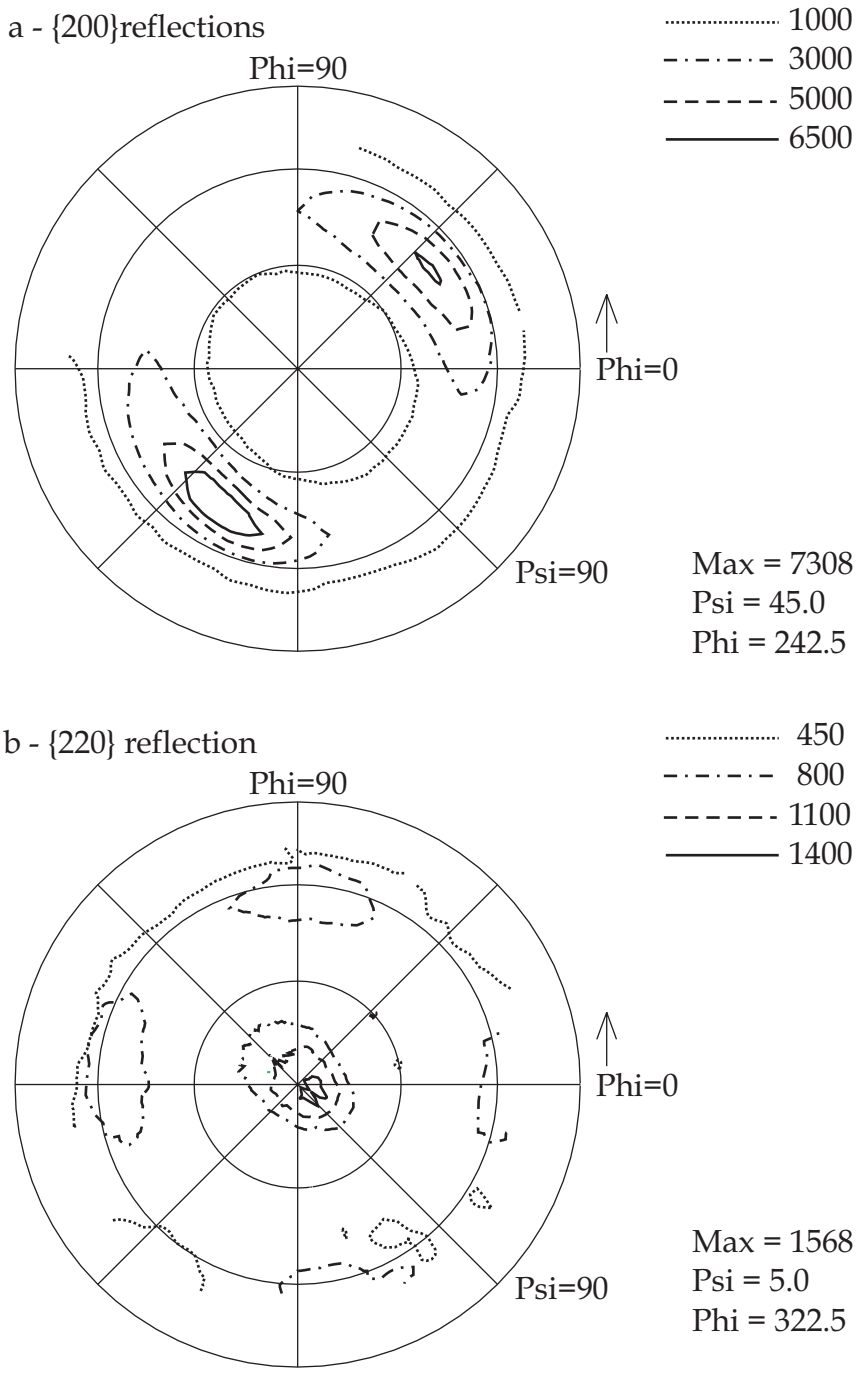

Figure 3.6 Pole figures of the {200} and {220} reflections of the specimen prepared at 55%Ti, -65V and 60 minutes. This is called a biaxial texture.

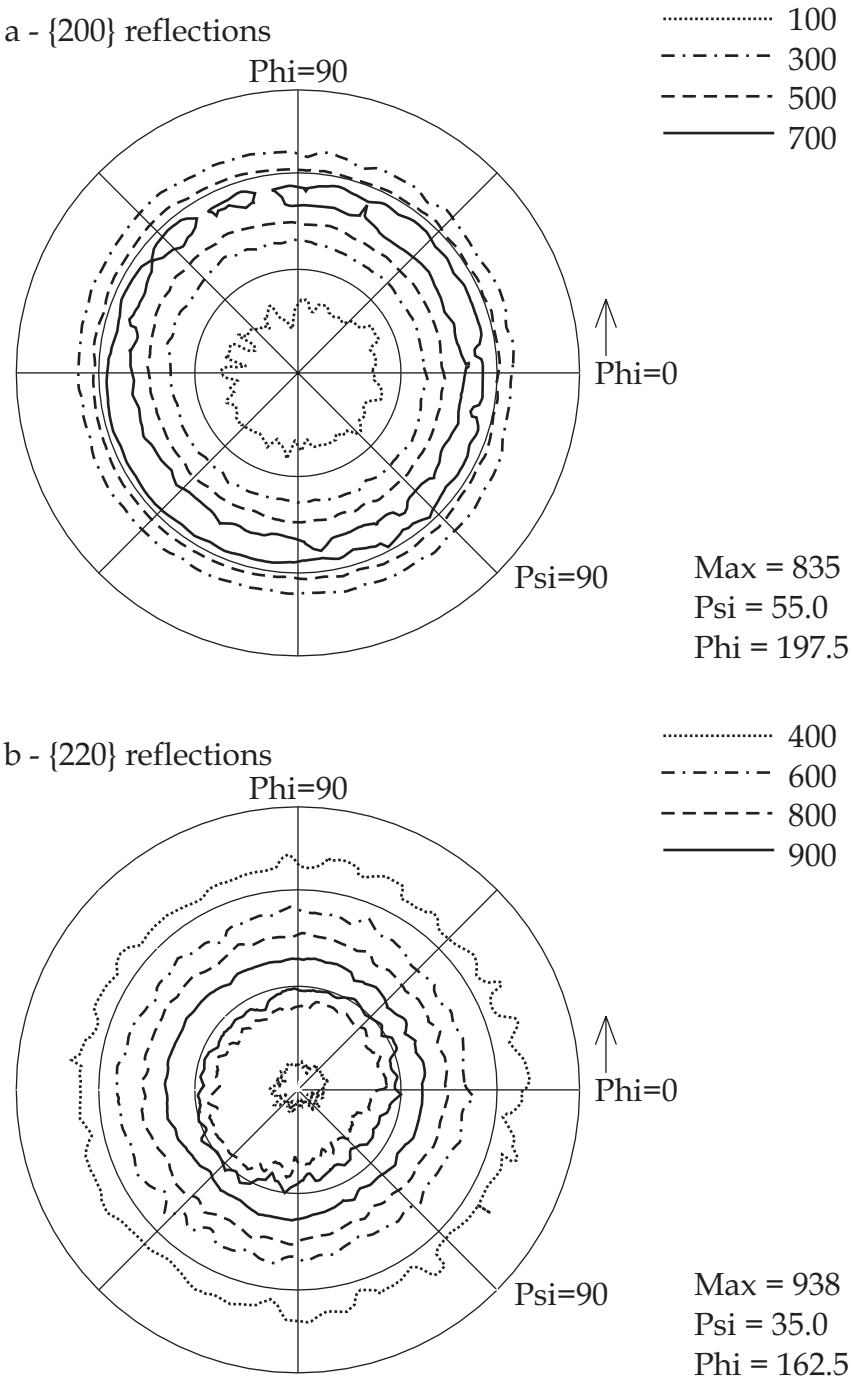

Figure 3.7 Pole figures of the {200} and {220} reflections of the specimen prepared at 50%Ti, -80V and 60 minutes. This is called a fibre texture.

In Figure 3.7 the intensities of the {200} and the {220} reflections of the specimen fabricated at –80V and a Ti concentration of 50% are plotted. This is clearly not a biaxial texture because there is no φ dependence. The ψ angle for which the {200} reflections have a maximum is 55°. The {220} planes show the same behaviour, no φ dependence. The maximum for this reflection is found at ψ=35°. The 55° and the 35° angles correspond with the {111} planes being parallel to the specimen surface. Due to the substrate reflections it is not possible to measure the intensity of the {111} reflections. This type of texture is called a {111} *fibre texture* because there is only a preference for the plane that lies parallel to the specimen surface but the directional dependency within this plane is not present. The change in texture towards a {111} fibre texture with increasing bias voltage is regularly observed [5]. The remaining two specimens, -40V 80% Ti and –80V 80% Ti, do not have a specific texture. This can be seen from the intensities of their {200} reflections presented in Figure 3.8.

Discussion

There are different physical aspects that strongly influence or even solely determine the texture evolution:

- Surface energy consideration [6].
- Minimising the strain energy [7].
- The influence of ion-bombardment and kinetic effects [8,9,10,11].

The surface energy of a plane can be calculated using the sublimation energy and the number of free bonds per surface area. For TiN the surface energy for the {111}, {220} and {200} planes are $4.0 \cdot 10^2$, $2.6 \cdot 10^2$ and $2.3 \cdot 10^2$ [J m^{-2}] respectively. (Sublimation energy is $6.5 \cdot 10^{-19}$ [J $atom^{-1}$] [6].) The {200} planes have the lowest surface energy and the influence of this surface energy is visible in textured TiN coatings prepared by chemical vapour deposition. The texture is for these CVD TiN coatings nearly always a {200} fibre texture because thermo-dynamic considerations determine the crystallographic orientation.

The total strain energy is proportional to the layer thickness and depends on the mean elastic moduli acting in the (hkl) plane parallel to the interface. The strain energy for a coating with biaxial equal principal stresses, a fibre texture and a thickness L is then given by:

$$U_{\{hkl\}} = \varepsilon^2 \cdot L \cdot \sum_{\{mno\}} E_{inplane}^{\{mno\}} \qquad (3.1)$$

(E is the Young's modulus and ε is the strain.) For a material with isotropic X-ray elastic constants, XEC, the strain energy will be independent of the orientation of the coating, it does not play a role in the texture development.

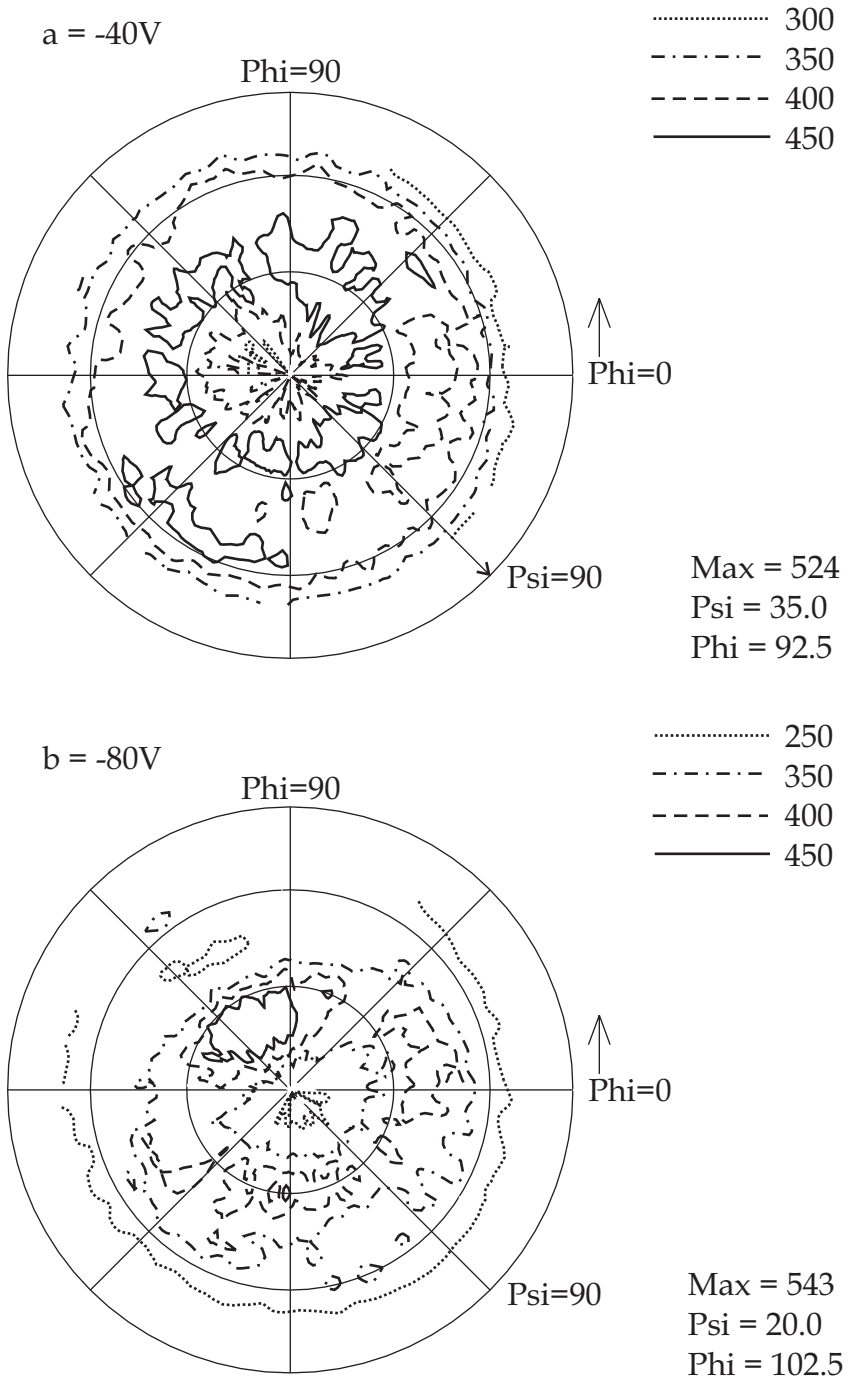

Figure 3.8 Pole figures of the {200} reflections of the specimens prepared at 80%Ti and 60 minutes and a bias voltage of -40 and -80V, respectively. There is no clear texture visible.

However, the XEC for TiN are very anisotropic and $S_2^{\{111\}} > S_2^{\{220\}} > S_2^{\{200\}}$. For TiN the strain energy is minimised when the {111} plane is parallel to the interface. Therefore, when the strain energy is the driving force the orientation will be a {111} fibre texture.

The strain in the deposit is proportional to the bias voltage, see section 3.2, and therefore at a higher bias voltage the influence of the strain energy will increase. This phenomenon is used in literature by Oh et al [7] to explain why in specimens with a higher strain, the first part of the layer has a tendency towards a {200} texture and that after a certain layer thickness this changes towards a {111} texture. The difference in strain energy between the {111} and the {200} planes is related to the layer thickness and the difference in surface energy is a constant value. If the layer is thin the surface energy is dominant but with increasing thickness the strain energy becomes more important and the texture will eventually change. However, the total energy increases when during the deposition the initial {200} texture changes towards a {111} texture. Therefore, this is energetically not favourable. Furthermore, in this reasoning the {220} plane was tacitly neglected. The {220} planes possess a surface energy that is much lower than the {111} planes but a strain energy that is almost the same. Consequently, a region with a {220} texture should be visible between the {200} and the {111}-oriented areas. However, this is not observed.

Other causes must induce the change towards the {111} fibre texture at elevated bias voltage and it may be possible that kinetic effects play the dominant role. As mentioned before, the increase in bias voltage results in an increase in ion current and more material is removed after deposition. This will put the emphasis on the growth rate of the different planes. However, at this stage it is not possible to give a satisfactory explanation for the change in texture with increasing bias voltage.

The biaxial texture is neither a {111} nor a {200} texture. So the major driving force behind the texture evolution is neither the strain nor the surface energy. This is supported by the fact that these effects would have resulted in a fibre texture, which is not the case. It seems reasonable to assume that the ion-bombardment and kinetic effects play the key-role in the development of the texture. For the ion-bombardment the selection mechanism for grain orientation is the difference in sputtering yield between crystallites. For misaligned crystals the energy dissipation of the bombarding ions will occur at the surface of the crystal. However for aligned crystals the dissipation occurs in the crystals, due to channelling. Therefore the resputtering is for aligned crystals lower than for misaligned crystals and this can result in the present biaxial texture [7]. This mechanism is also used to change the {111} fibre texture into a single crystal orientation. Bombarding a growing film with high-energy ions under a ψ angle of 54.7° in one φ direction will result in a single crystal texture [11].

It is hard to say why the specimens fabricated at a titanium concentration of 80% have an undefined texture. However, it seems reasonable that the concentration of titanium and nitrogen has an influence on the crystallographic texture because the surface energy and strain energy will be influenced by the exact stoichiometry of the film.

3.2 Macro residual stresses

Measuring the position of a Bragg reflection as a function of its orientation enables one to determine the macro residual stress present in a specimen. However, it is necessary to perform certain corrections before the true reflection position can be determined. The main corrections are a background correction, only necessary when the background increases or decreases with the 2θ angle, and a subtraction of the $K\alpha_2$ to obtain the clean $K\alpha_1$ radiation. It is now possible to calculate the lattice spacing using Bragg's law. With this lattice spacing and the unstrained lattice spacing the strain can be determined. If the unstrained lattice spacing is unknown the procedure is to use the value at ψ=0 instead of the d_0. In most cases this only generates a small error in the outcome.

Before starting the measurements, it is meaningful to reflect upon the origin of the strain. The strain in magnetron sputtered layers* originates from the thermal strain [12] and the atomic peening strain [13,14,15]. The thermal strain is a consequence of the difference in thermal expansion coefficients between the substrate and coating, and the difference in deposition and room temperature:

$$\varepsilon^{thermal} = \Delta\alpha \cdot \Delta T \tag{3.2}$$

The thermal strain for a TiN layer on a hard metal is tensile and is approximately $5.9 \cdot 10^{-4}$. This is derived from an expansion coefficient for TiN of $\approx 8.6 \cdot 10^{-6}$ [K^{-1}] [16] and for WC of $\approx 6.8 \cdot 10^{-6}$ [K^{-1}] [17]. The deposition temperature was 620 K.

The incoming atoms and ions, due to their high kinetic energy, generate a hydrostatic stress in the coating, which induces an expansion of the coating [18]. This is called the atomic peening strain. To make it possible to fit the layer onto the infinitely stiff substrate, it is necessary to apply a compressive biaxial strain. So, depending on the magnitude of the peening strain, the resulting strain in the layer will be either tensile or compressive.

* There are other mechanisms, like a lattice mismatch between the substrate and the film or film porosity, that can induce a strain in sputtered film. However, these do not play a role in the magnetron sputtered films studied in this thesis.

3.2.1 Strain measurements

The relation between the strain in the laboratory and the specimen frame is covered by Equation (2.13). The strain in thin films is in general biaxial and two terms in Equation (2.13) disappear resulting in:

$$\varepsilon_{33\ (\varphi\psi)}^{Lab} = \frac{d_{\varphi\psi} - d_0}{d_0} = \left[\varepsilon_{11}\cos^2\varphi + \varepsilon_{12}\sin 2\varphi + \varepsilon_{22}\sin^2\varphi - \varepsilon_{33}\right]\sin^2\psi + \varepsilon_{33} \qquad (3.3)$$

Although, see chapter 2, for specimens with a biaxial strain it is in principle only necessary to perform the strain measurements in two φ directions the measurements here are carried out in three different φ directions.

The position of the {220} reflections is measured as a function of the ψ angle, and the three different φ directions are determined in relation with the biaxial texture. The different φ directions are:

1. The rolling direction (RD), that is the [2$\underline{2}$0] direction.
2. The transverse direction (TD), this is the direction perpendicular onto the rolling direction.
3. A direction making 45° with both these directions. Called from now on the bisecting direction, BD.

The reason for choosing the {220} reflection is that the other diffraction peaks showed either an oscillating d–$\sin^2\psi$ behaviour or the intensity was too low to obtain a proper diffraction peak. (The cause of the non-linear d-$\sin^2\psi$ will be investigated in chapter 4.) From the slope of the d-$\sin^2\psi$ plot it is possible to determine the ($\varepsilon_{11}\cos^2\varphi + \varepsilon_{12}\sin 2\varphi + \varepsilon_{22}\sin^2\varphi - \varepsilon_{33}$) term. The latter is called the *strain term* in the remainder of this section.

First, the specimens from batch 1 are investigated. Figure 3.9 shows that the strain in all the specimens is smaller than the calculated thermal strain, $6\cdot10^{-4}$. The difference is due to the already mentioned atomic peening process. The compressive strain in the 40% and 80% specimens, which have a different denser surface structure, is clearly larger than the strain in the other specimens.

This can be explained by considering the relation between the deposition parameters and the atomic peening. The atomic peening strain is given by [3]:

$$\varepsilon = B \cdot \frac{J_{ions} \cdot N_i}{J_{atoms}} \qquad (3.4)$$

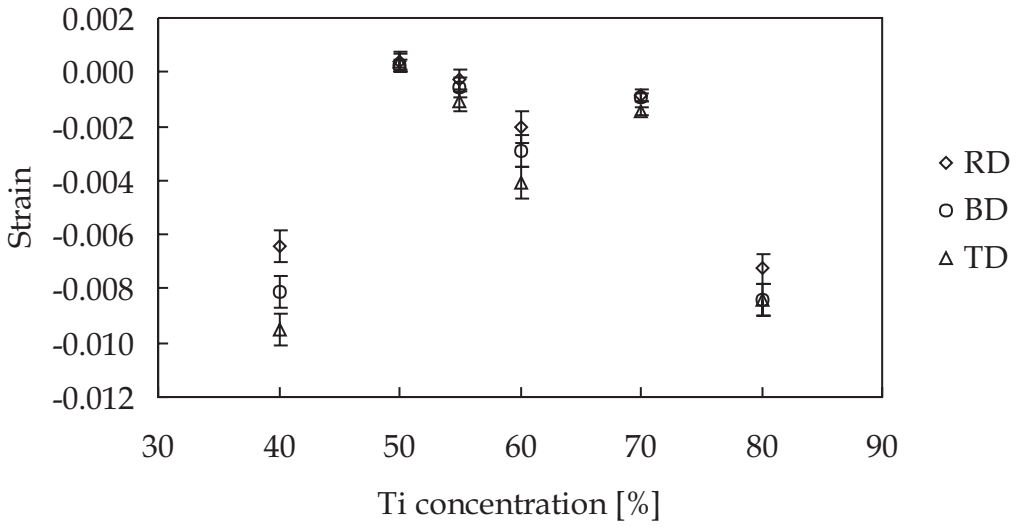

Figure 3.9 Strain distribution in the specimens from the first batch. Only for the last specimen does the relation |TD|>|BD|>|RD| not hold.

With N_i the number of interstitials produced per bombarding ion and B is a constant. It seems not very plausible to assume that the number of interstitials per ion will change as the Ti concentration is varied. Therefore, the change in concentration must change the ratio of flux of ions and atoms. This is in agreement with the change in morphology visible in these two specimens, which can also be caused by a change in J_{ions}/J_{atoms}. By decreasing the titanium concentration, the amount of titanium ions in the plasma will decrease and assuming, that, the number of ions is linearly proportional to the titanium concentration makes it possible to substitute the J_{ions} by the titanium concentration. The growth rate can be derived from the deposition time and the film thickness. However, for all the specimens the deposition time was the same and J_{atoms} may be replaced by the layer thickness. The ratio, J_{ions} over J_{atoms} can now be calculated, see Table 3.2. Comparing these values with the measured strain shows the same trend: a higher compressive strain a larger J_{ions}/J_{atoms}. The

Table 3.2 Layer thickness and ratio J_{ions} over J_{atoms} for batch1

Ti concentration [%]	Layer thickness [μm]	J_{ions}/J_{atoms}
40	1.9	21
50	3.0	17
55	3.1	18
60	3.2	19
70	4.0	18
80	4.2	19

absolute values are difficult to compare because the linear relation between the Ti concentrations and the ions is just an assumption and the influence of argon ions is completely neglected. It is now also clear why the microstructure of the 40 and 80% specimens differs from the other specimens of the batch.

Taking a closer look at the relation between the texture and the strain distribution shows that for the specimens with a biaxial texture, Ti concentration of 40, 50, 55, 60 and 70%, the absolute value for the transverse direction is higher than for the bisecting direction, which is again higher than, the rolling direction. This is not clearly visible for the specimen prepared at a Ti concentration of 50%, the reason for this is that the strain term is almost equal to zero. For one specimen from the first batch this relation is not present and that is the specimen prepared at 80% titanium. This is also the specimen, which does not have a biaxial texture.

The strain measurements carried out on the specimens from the second batch, Figure 3.10, show that when the deposition time is increased the strain term decreases. The measured strain is an average over the irradiated volume where the main contribution is coming from the top of this volume. Assuming that the strain is highest at the interface and decreases towards the surface can explain the experimental data.

The growth speed is for the four specimens the same. Therefore, J_{atoms} is not changing during the deposition and the decrease in strain must be due to a change in J_{ions} or a relaxation process must take place. However an explanation

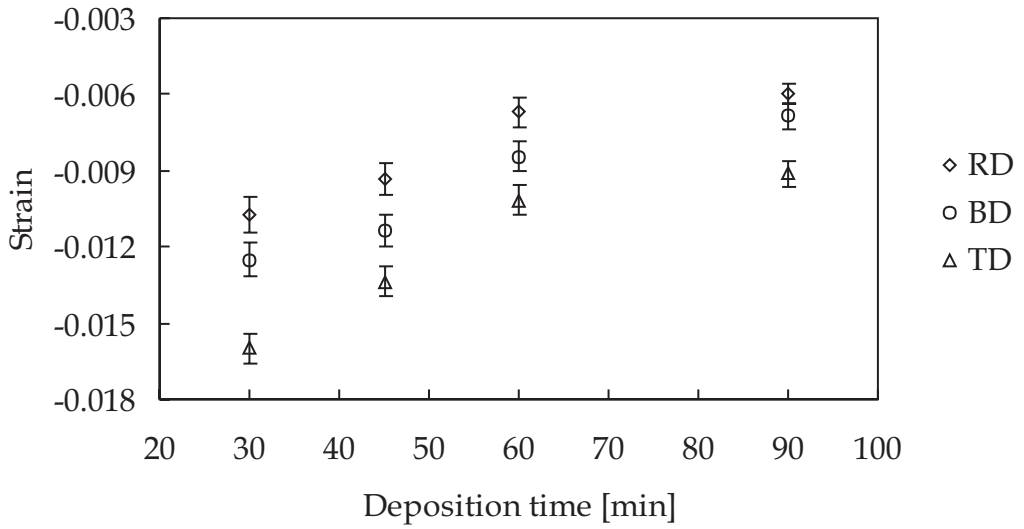

Figure 3.10 Strain distribution in the specimens from the second batch. For all the specimens |TD|>|BD|>|RD| holds.

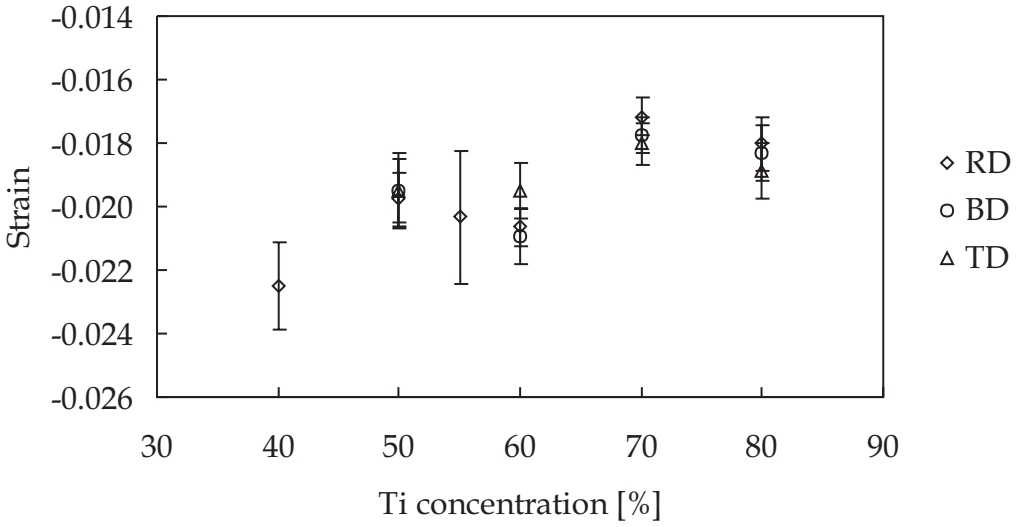

Figure 3.11 Strain distribution of the specimens from the third batch. No relation between the directions.

for this phenomenon is at present not known. Investigation into the relation between the strain distribution and the texture, all the specimens have a biaxial texture, gives the same relation as for the biaxial textured specimens from the first batch. The strain term in the transverse direction is higher than in the bisect direction, which is again higher than in the rolling direction.

Finally, the strain terms of the specimens from the third batch are determined, Figure 3.11. The strain is much higher than for the first and the second batch. This is due to the higher bias voltage, which enhances the kinetic energy of the incoming particles. The result of this is that the peening ratio increases significantly. The relation between the strain and the Ti concentration is comparable to that of the first batch. For only four specimens, the strain term is determined in three different φ directions. There appears to be no relation between the strain term and the φ direction. This is the case for all the specimens, i.e. the three specimens with a fibre texture and the specimen without a specific texture.

Conclusions

From the investigation of the relation between the texture and the strain distribution two conclusions can be drawn:

1. Whether or not there is a relation between the strain and the φ angle is determined by the kind of texture present in the layers. When the texture depends on the φ angle the strain does as well.

2. There is a relation between the asymmetrical strain distribution and the strain generating mechanism.

3.2.2 X-ray elastic constants and texture

The strain in sputtered layers has two causes: a thermal origin and the atomic peening process. Assuming that the expansion coefficients of the substrate and the coating are isotropic and that the coating is a polycrystalline material without a texture, then the strain distribution will be rotational symmetric, $\varepsilon_{11}=\varepsilon_{22}$ and the $\varepsilon_{12}=0$. The same is true for the atomic peening process; the peening will result in an expansion of the unit cell, which will be independent on the orientation of the cell. This increase in volume is restricted by the substrate and a strain is introduced in the coating. For a polycrystalline material without a texture, this will result in a uniform strain.

The question that has to be addressed is what happens in a material with a specific texture and anisotropic XEC? Consider a cubic single crystal, which is oriented with the [002] and the [2$\bar{2}$0] directions perpendicular to the surface normal. The [002] direction is defined as the x-direction and the [2$\bar{2}$0] as the y-direction. To match the expanded crystal onto the substrate it is necessary to apply a force. For a material with isotropic elastic compliances the forces in the x and y directions are the same and therefore the stresses are the same. However, when the material is anisotropic the stress fields in the x- and y-directions are not the same.

For cubic materials there are only three independent elastic compliances; S_{11}, S_{12} and S_{44} and with the equation $2*(S_{11}-S_{12})/S_{44}$ it is possible to calculate the anisotropy factor of a material [19]. These three compliances also define the Young's modulus and the Poisson's ratio of the {hkl} planes, using Reuss's approximation, according to:

$$E_{\{hkl\}}=\frac{1}{S_{11}-2\cdot\Gamma_{\{hkl\}}\left(S_{11}-S_{12}-\frac{1}{2}S_{44}\right)} \tag{3.5}$$

$$\nu_{\{hkl\}}=-\frac{S_{12}+\Gamma_{\{hkl\}}\left(S_{11}-S_{12}-\frac{1}{2}S_{44}\right)}{S_{11}-2\cdot\Gamma_{\{hkl\}}\left(S_{11}-S_{12}-\frac{1}{2}S_{44}\right)} \tag{3.6}$$

These equations are derived from Equations (2.24), (2.26) and (2.27) with the gamma defined by Equation (2.29). The relation between the strain of the {hkl} planes in the laboratory system and the stresses in the specimen system reads:

$$(\varepsilon_{33}^{'})_{\varphi\psi} = \frac{d_{\varphi\psi} - d_0}{d_0} = \left(\frac{1+\nu}{E}\right)_{\{hkl\}} \left[\sigma_{11}\cos^2\varphi + \sigma_{22}\sin^2\varphi\right]\sin^2\psi - \left(\frac{\nu}{E}\right)_{\{hkl\}} \left[\sigma_{11} + \sigma_{22}\right] \quad (3.7)$$

It is now possible to calculate the ratio between the stresses in the [002] and the [2$\underline{2}$0] direction for the single crystal mentioned above. The strain components in the x and y direction, ε_{11} and ε_{22}, must be equal and this will result in a ratio between the stresses in the [200] and the [022] direction given by:

$$\frac{\sigma_{11}}{\sigma_{22}} = \left(\frac{E}{1+\nu}\right)_{\{200\}} \cdot \left(\frac{1+\nu}{E}\right)_{\{220\}} \cdot \frac{\varepsilon_{11} - \varepsilon_{33}}{\varepsilon_{22} - \varepsilon_{33}} \quad (3.8)$$

For a coating with a fibre texture and for a layer without a texture, the average E modulus in a plane parallel to the interface is independent of the φ angle. However, this is not necessarily the case for a material with a biaxial texture and it is possible that the stresses σ_{11} and σ_{22} are different.

In the specimens with a biaxial texture, most crystals are oriented with the (220) plane parallel to the interface and the [2$\underline{2}$0] axis in the rolling direction and their [002] axis in the transverse direction. The anisotropy factor for TiN is smaller than 1, $E_{\{200\}} > E_{\{220\}}$. So the average elastic modulus in the transverse direction is higher than in the rolling direction. Consequently, the force being applied in the transverse direction must also be larger than in the rolling direction. This will result in a difference in lattice spacing between the {220} planes measured in the transverse and in the rolling direction.

The strain distribution is a result of the anisotropy of the elastic compliances and the biaxial texture and it must be possible to make an estimate of this value. First the ratios between the measured strain in the transverse and in the rolling direction are calculated, which gives an average value of 1.47. Because the layer is polycrystalline with a specific texture and not a perfect single crystal the measured ratio must be smaller than the ratio calculated with Equation (3.8). This is due to the averaging of different oriented grains. Taking the upper values from literature: S_{11} =1.8·10^{-12} S_{12} = -3.76·10^{-13} and S_{44} = 6.2·10^{-12} [20,21], gives an anisotropy factor of 0.7 and calculating the ratio between the <200> and the <220> direction results in a ratio of 1.32. As mentioned before this value must be larger than the measured one, but instead it is smaller than the measured ratio of 1.47. Assuming that S_{11} =1.8·10^{-12}, S_{12} = -3.2·10^{-13} and S_{44} = 8·10^{-12}, and using Equation (3.8) again to calculate the ratio between the <200> and <220> directions, result in a value of 1.67. This value is indeed larger than the measured ratio of 1.47. Using these compliances to calculate the anisotropy factor gives a value of 0.53.

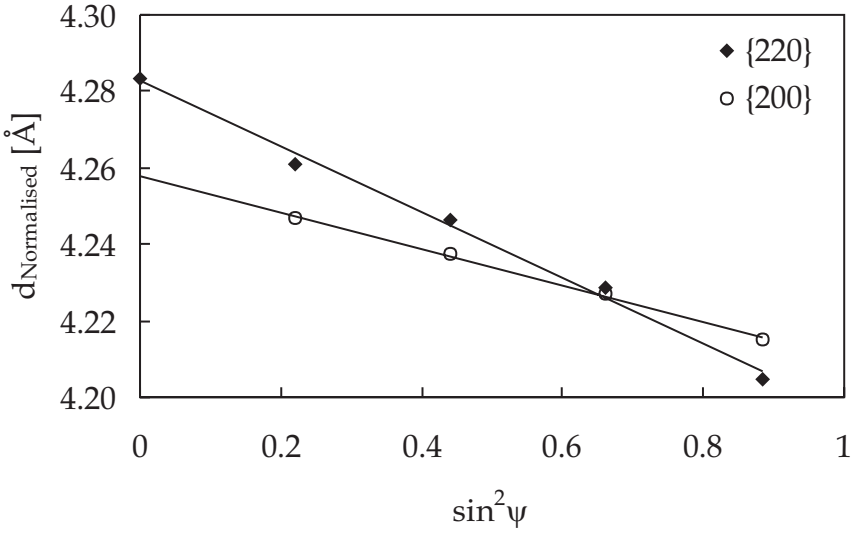

Figure 3.12 Difference in slope for different reflections due to the anisotropic XEC.

When the anisotropy is as large as calculated, then this should also be visible in the specimens with a symmetrical strain distribution. Diffraction measurements at the same φ angle but using different diffraction peaks should give a difference in strain between the different planes. This is a consequence of the stress equilibrium, which must exist in the same direction between differently oriented adjoining grains (Reuss's approximation). Using Equation (3.7) to calculate the stresses from the measured strain should give the same value for the different diffraction planes. (This is called the quasi-isotropic approach [21]) The ratio between the strain term of the different diffraction planes is then again given by Equation (3.8). The lattice spacing of the {200} and the {220} planes of a specimen from the third batch are plotted in Figure 3.12 (d spacing normalised to d_0). The slope of the {200} planes is considerably lower than the slope of the {220} planes. This is in agreement with the assumption of a high anisotropy. The difference between the {200} and {220} plane is 1.76, and this is a little larger than the value calculated with Equation (3.8), which is 1.67. The difference can be a consequence of the fact that the data are obtained at different 2θ values. When the 2θ increases, the penetration depth increases as well. Due to strain gradient [18], this will automatically result in a difference between the different planes even when correct XEC are being used.

Conclusions

The macro residual stress in TiN magnetron sputtered coatings is mainly compressive. Increasing the bias voltage results, in the investigated bias area, in

an increase in macro stress. Also the Ti concentration has an influence on the size of the macro residual stress. Both phenomena can be explained with the ratio of ions over atoms that impinge on the surface. The macro stress is also found to decrease with increasing layer thickness, the cause for this is not known. The strain distribution in the specimens is related to the crystallographic texture and from this and quasi-isotropic strain measurements the elastic compliances are determined. TiN is elastically a very anisotropic material.

3.3 Position and shape of diffraction peaks

3.3.1 Instrumental broadening.

It was mentioned in section 2.2.5, that the shape of a diffraction peak information contains about the grain size and the deformation strain in a specimen. However, before it is possible to obtain this information it is necessary to determine the instrumental broadening of the X-ray equipment. The instrumental broadening manifests itself in the fact that a measurable peak width is obtained even when a single crystal without defects and infinitely large for the X-rays, that is larger than 1000Å, is considered. According to the literature [22], the optimum standard specimen for X-ray diffraction line-profile analysis is a NIST Si powder. In this section, a specimen of sintered ferrite is used to determine the instrumental broadening. One of the advantages of ferrite is its high mass absorption so no transparency broadening will occur. The results will be compared with the results of Si powder from literature.

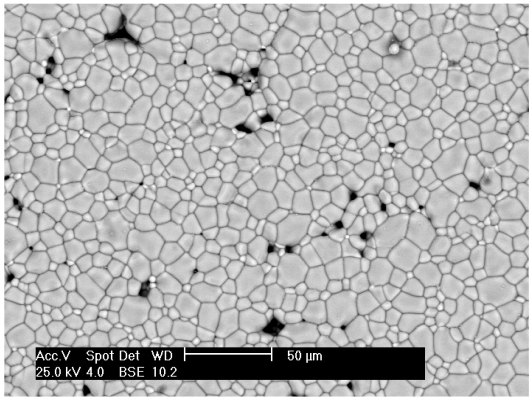

Figure 3.13 Plane view BSE micrograph of $Mn_{0.67}Zn_{0.25}Fe_{2.08}O_4$ Ferrite.

Ferrite is a ceramic material and is produced by dry-pressing iron, manganese and zinc oxides in round pellets. (Fe_2O_3 71.0 weight %, MnO 20.3 weight % and ZnO 8.7 weight %). These pellets are then sintered in a conditioned oxygen environment. The outcome is a ferrite with a chemical composition given by $Mn_{0.67}Zn_{0.25}Fe_{2.08}O_4$ and with an average grain size of 7 μm. (See Figure 3.13.) The 7 μm ensures that even with a Gaussian distribution around this value the grain size is in the desired range, 1 to 10 μm, i.e. an infinite size for the X-rays.

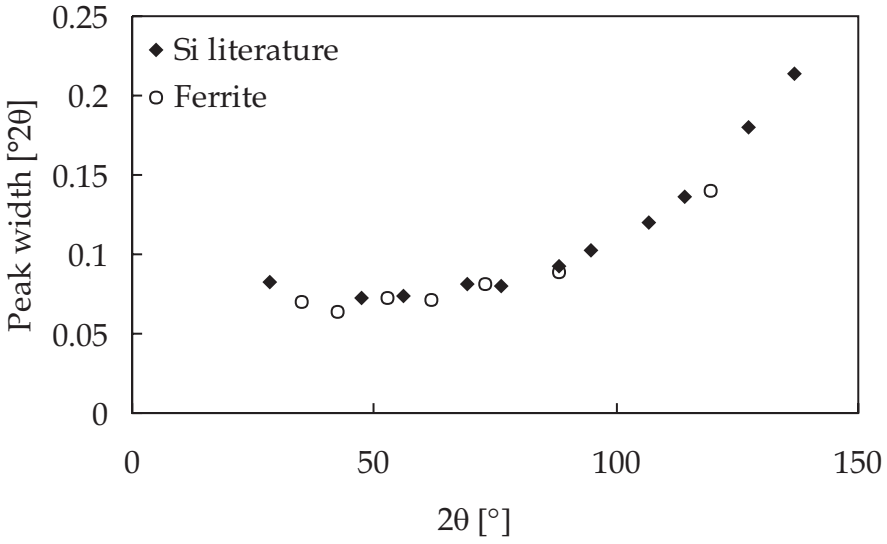

Figure 3.14 Instrumental broadening for ferrite and silicon powder. The data of the silicon powder are obtained from literature.

The conditions under which the measurements are performed are presented in Table 3.3. From the diffraction pattern of the ferrite the peak width of the $K\alpha_1$ reflections are determined. The peak widths of the reflections of the two specimens are compared in Figure 3.14. The results obtained with the ferrite give the same amount of broadening as the data from literature. Therefore, it seems permissible to use the ferrite specimen to correct for instrumental broadening during X-ray diffraction line profile analysis. All the measurements within this dissertation that are used for the analysis of the line profile are carried out under the same conditions as tabulated in Table 3.3. The function that is used to correct for the instrumental broadening is given by:

$$\beta_{instrumental} = 1.24 \cdot 10^{-5} (2\theta)^2 - 1.08 \cdot 10^{-3} (2\theta) + 9.14 \cdot 10^{-1} \qquad (3.9)$$

With the broadening in °2θ.

Table 3.3 Settings used for measuring the instrumental broadening

	NIST Si powder	Ferrite
Diffractometer	Siemens D500	Philips1730
Voltage [kV]	45	40
Current [mA]	30	30
Divergence slit [°]	1	1
Scatter slit [°]	1	1
Receiving slit [°2θ]	0.018	0.017
Diffracted beam soller slits [mm]	0.001765	

3.3.2 Lattice spacing, strain broadening and grain size

The intensity of a reflection and the presence of substrate peaks in its vicinity determine whether a reflection is suitable for the analysis of its profile. The intensity varies and the influence of this must be assessed for each specimen and reflection. The influence of substrate peaks can be determined by comparing a diffraction pattern of a bare and of a coated substrate (Figure 3.15).

The hexagonal tungsten carbide has many reflections, which reduces the number of available TiN peaks considerably. The reflections for which the peak positions can be determined with reasonable accuracy are the {111}, {200}, {220}, {222}, {400}, {331} and the {422} (Intensity considerations neglected.) The

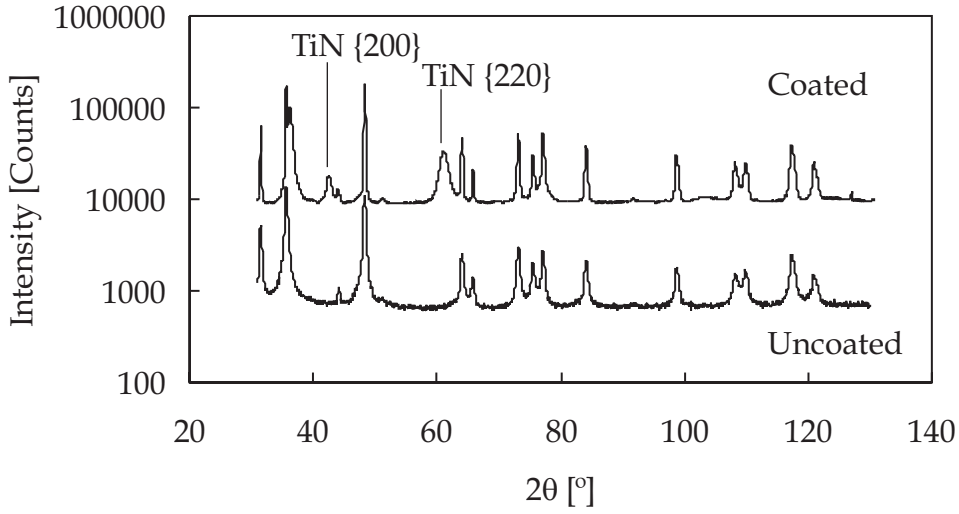

Figure 3.15 Diffraction pattern of the coated and of the uncoated substrate. The same diffractometer setting are used.

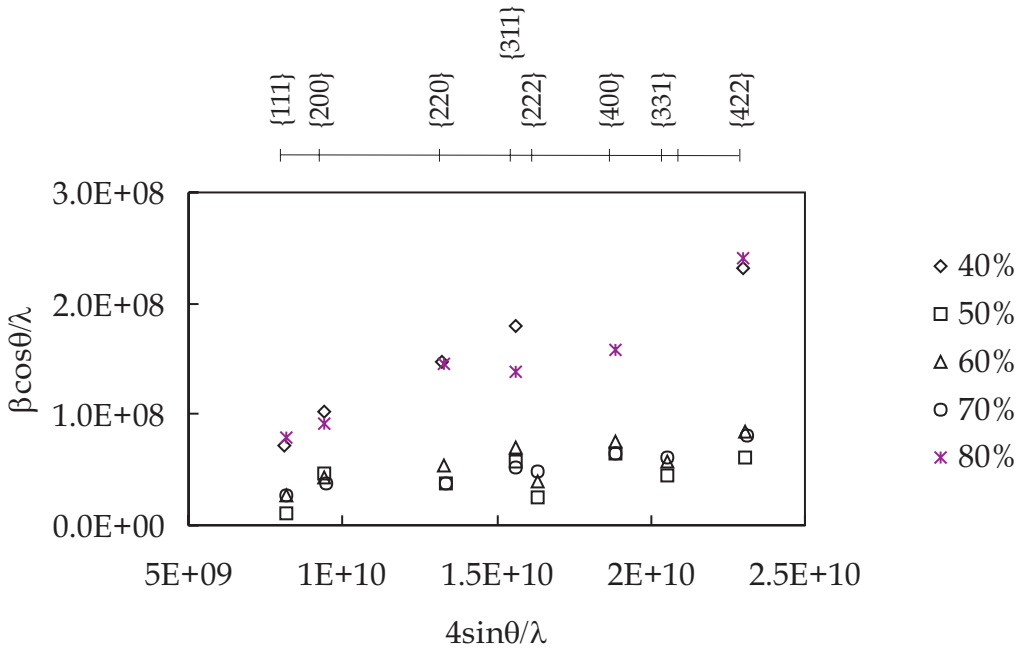

Figure 3.16 Williamson-Hall plots for the specimens from batch 1 for which the Ti concentration was varied. There is a large difference between the 40 and 80% specimens in comparison with the 50, 60 and 70% specimens.

broadening is determined for the {111}, {200}, {220}, {400}, {331} and the {422} reflections.

Batch 1

Williamson-Hall, section 2.2.5, plots of the specimens prepared at –40V are presented in Figure 3.16 and the intercept and slope of the lines that reflects the trend are tabulated (Table 3.4). The most remarkable point is that the specimens with the highest compressive stresses, 40 and 80% titanium, have a slope that differs from the other specimens. So, at first sight there appears to be a relation between the macro residual stress and the deformation strain.

Table 3.4 Deformation strain, grain size and d_0 of the specimens of batch 1

	Titanium concentration [%]				
	40	50	60	70	80
ε_{hh}	$1.1 \cdot 10^{-2}$	$2.3 \cdot 10^{-3}$	$3.1 \cdot 10^{-3}$	$3.2 \cdot 10^{-3}$	$9.8 \cdot 10^{-3}$
Intercept [m^{-1}]	$-5.9 \cdot 10^{7}$	$1.0 \cdot 10^{7}$	$1.0 \cdot 10^{7}$	$1.7 \cdot 10^{6}$	$-1.7 \cdot 10^{6}$
d_0 [Å]	4.2573	4.2432	4.2477	4.2417	4.2548

According to theory, it is possible to determine the grain size from the inverse of the intercept. It is readily seen that this results in an unreliable value. The 40 and 80% Ti specimens have a negative intercept, which has no physical meaning. Also the error in the intercept is large, $\approx 1 \cdot 10^7$, in comparison with the value itself.

The theory also predicts a linear relation between the $\beta \cdot \cos\theta / \lambda$ and the $4\sin\theta / \lambda$, but there is a deviation visible for the specimens with a smaller slope. One should realise that when the profiles of the different reflections are compared one compares different grains. In the previous section, it was shown that there is a texture present in the coating. The driving forces behind this texture may have an influence on the grain size and on the deformation strain in the different oriented grains. This may influence the results considerably.

Very briefly, we will make some remarks about the d_0 determined from the measured d spacings using a Nelson-Riley plot, section 2.2.3. Figure 3.17 shows the result for two specimens: 70 and 80% Titanium and this confronts us with the difference in macro residual stress. The macro residual stress has a structural influence on the lattice spacing at $d_{\psi=0}$. This value is not $d_0^{\{hkl\}}\sqrt{(h^2+k^2+l^2)}$ but changes to:

$$d_0^{\{hkl\}}\sqrt{h^2+k^2+l^2} + 2d_0^{\{hkl\}}\sqrt{h^2+k^2+l^2}S_1^{\{hkl\}} \cdot \sigma \qquad (3.10)$$

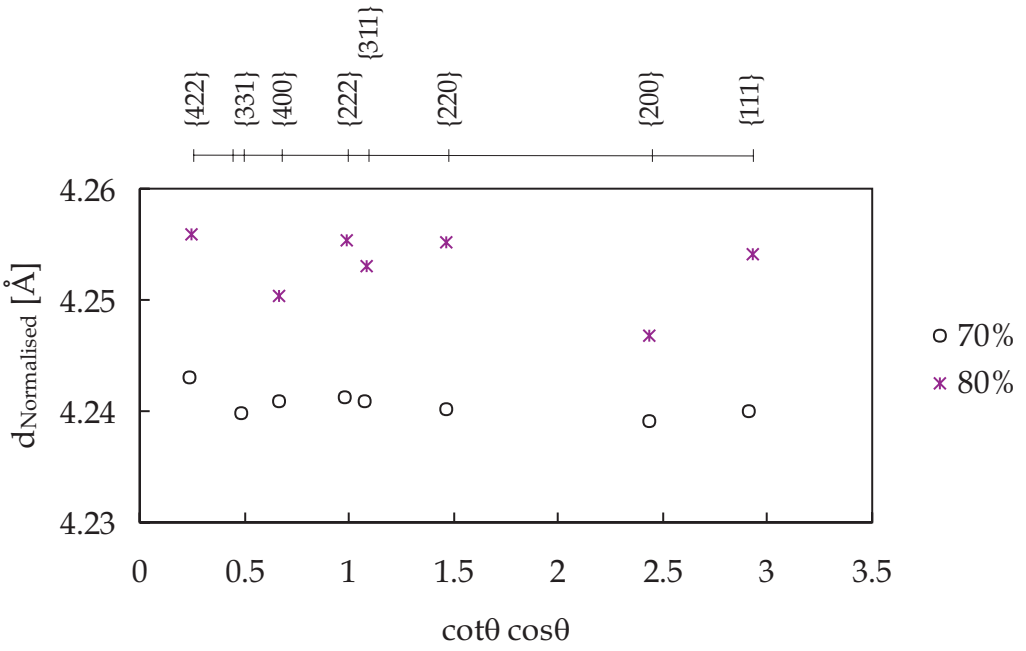

Figure 3.17 Nelson-Riley plots for two specimens of batch 1 for which the Ti concentration was varied. The difference in absolute value between the two specimens is a result of the difference in macro residual stress.

This can be derived from Equation (3.7). The measured $d_{\psi=0}$ depends thus on the size of the macro residual stress. However, also the dispersion around the fit through the points is larger for the 80% specimen than for the 70% specimen. The macro residual stress is partially responsible for this dispersion. Assuming the stress is constant then the theoretical value obtained for a specific reflection will depend on the XEC $S_1^{\{hkl\}}$. When the XECs are anisotropic the theoretical value for the lattice spacing will differ for different planes and the magnitude will depend on the magnitude of the macro residual stress. In theory it is thus possible, to determine the unstrained lattice spacing using the lattice spacing determined from the Nelson-Riley plot, the macro residual stress and Equation (3.10).

The change in Ti concentration has an influence on the chemical composition of the coating. This compositional change will influence the unstrained lattice spacing [23]. Therefore, it might be possible to determine the composition from the calculated unstrained lattice spacing. The problem in calculating this "unstrained lattice spacing" is the accuracy. The XEC and the strain are experimental values and possess as such an error. Due to the nature of Equation (3.10), the outcome is extremely sensitive to such errors. Neglecting the error in the measured lattice spacing and assuming an error of 5% in both the XEC and the strain result in an error in the unstrained lattice spacing of ≈0.005 Å. For TiN this leads to an error in the chemical composition of over 10 atom% and is not very reliable.

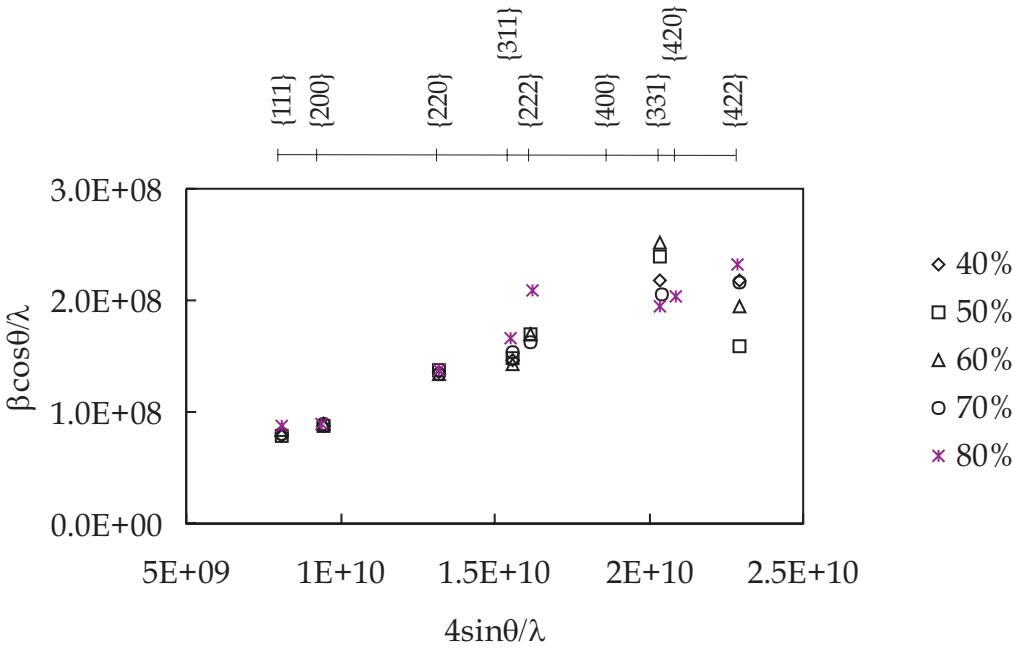

Figure 3.18 Williamson-Hall plots for the specimens from batch 3 for which the Ti concentration was varied. There is no large difference visible between the different specimens.

Table 3.5 Deformation strain, grain size and d_0 of the specimens of batch 3

	Titanium concentration [%]				
	40	50	60	70	80
ε_{hh}	$1.02 \cdot 10^{-2}$	$1.00 \cdot 10^{-2}$	$1.08 \cdot 10^{-2}$	$9.6 \cdot 10^{-3}$	$1.0 \cdot 10^{-2}$
Intercept [m^{-1}]	$-4.6 \cdot 10^{6}$	$-4.8 \cdot 10^{6}$	$-7.6 \cdot 10^{6}$	$2.6 \cdot 10^{6}$	$-2.9 \cdot 105$
d_0 [Å]	4.2667	4.2689	4.2699	4.2655	4.2739

Batch 3

The peak position and profile of the specimens from the third batch are also measured. From the peak positions and widths Williamson-Hall plots are generated, see Figure 3.18. The data are also presented in Table 3.5. There is no large difference visible in deformation strain between the different specimens within this batch. When the results are compared, with the strain broadening measurements from batch 1 then the values are comparable with the results found for the 40 and 80% specimens. However, looking at the relation between the macro stress and the deformation strain then the macro stresses in the specimens from the third batch are much higher than the macro stresses in the 40 and 80% specimens from the first batch. Initially there appeared to be a

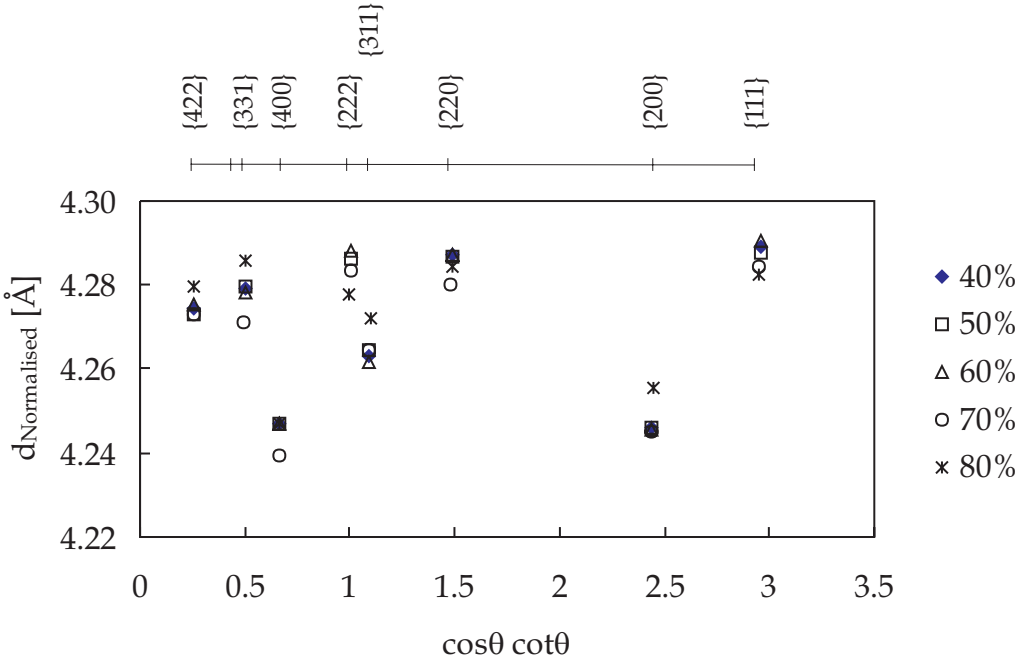

Figure 3.19 Nelson-Riley plots for the specimens from batch 3 for which the Ti concentration was varied. No large difference is visible between the specimens. However, there is a large dispersion between the different planes and especially between the {h00} and the {hhh} planes.

relation between the deformation strain and the macro stress. Yet the increase in macro stress and the deformation strain are not directly related. Therefore, the mechanism that generates the compressive stresses is not responsible for the strain broadening. It is for the specimens from this batch also very unreliable to use the intercept to calculate the grain size. The reason is the same as for the first batch, i.e. a negative intercept is found for some of the specimens.

The Nelson-Riley graphs, Figure 3.19, show a large difference in lattice spacing between the {111} and the {200} planes. This phenomenon supports the idea that TiN has a large anisotropy in the XEC. The determined lattice spacings at 2θ=180° are larger than the values from the first batch. This is again a result of the higher macro residual stresses that are present in the specimens from this third batch.

Discussion

To deduce information about the deformation strain and grain size using diffraction profiles is not a straightforward procedure. This can be concluded from the results presented above which show negative intercepts and deviation from a linear relation between the $\beta\cdot\cos\theta/\lambda$ and the $4\sin\theta/\lambda$. These deviations may be a result of the crystallographic texture, which may result in a grain size and or deformation strain that is orientation dependent. Besides this, it is also known that concentration variations, a macro stress gradient and the XEC may influence the outcome of the grain size and strain broadening experiments. Here a short study into the influence of the XEC, determined in the previous section, on the grain size and deformation strain is executed. The influences of the other phenomena are studied in chapter 4.

Assuming the maximum stress is independent of direction, then the maximum value of e_{hh} will be the maximum stress p_{max} divided by the appropriate value of the Young's modulus and Equation (2.19) changes into:

$$\beta\cdot\cot\theta = 4p_{\max}\left[S_{12}+2S_{44}+\left(S_{11}-S_{12}-2S_{44}\right)\frac{\left(h^4+k^4+l^4\right)}{\left(h^2+k^2+l^2\right)^2}\right] \tag{3.11}$$

In Figure 3.20 the calculated Williamson-Hall plots are presented. The points are calculated using Equation (3.11) and (2.21-b) assuming a grain size of 100 nm and a maximum tensile stress of 3.5 GPa. For the diamonds the mechanical XEC are used to calculate the broadening. (Mechanical XEC can be calculated using a constant value for the gamma, Γ=1/5 [24].) For the circles the normal XEC are used, calculated from the elastic compliances determined in section 3.2. Remarkable is the result of the linear fit through the points assuming

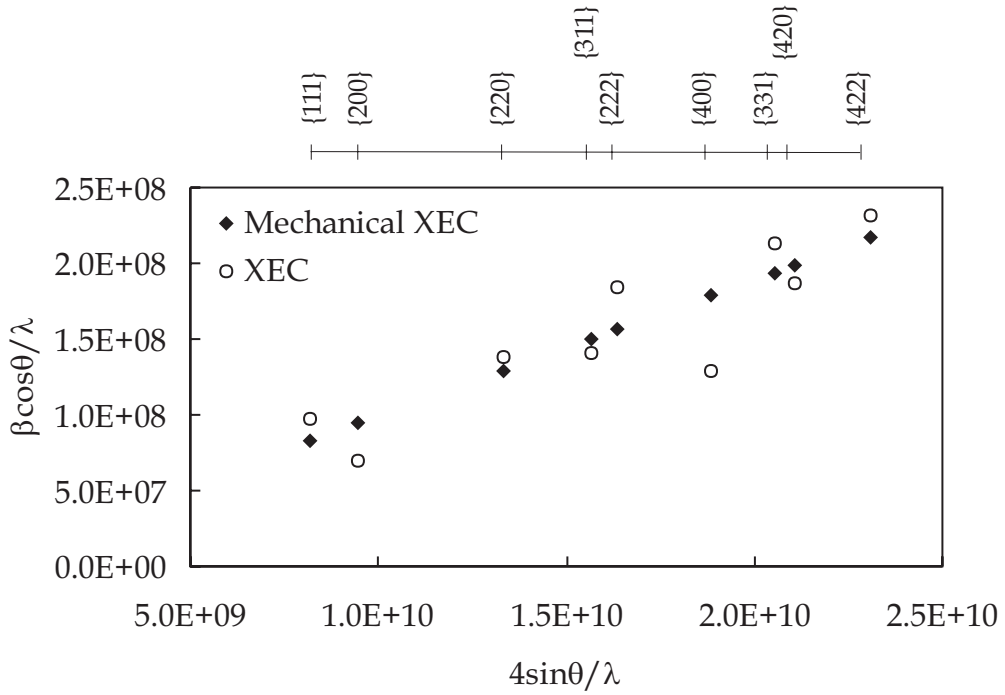

Figure 3.20 Influence of anisotropic XEC on the WH plot. Using the anisotropic XEC instead of the mechanical XEC results in a change of the intercept with the ordinate.

anisotropic XEC, which differs from the result obtained fitting a line through the points calculated using the mechanical elastic constant, Table 3.6. This difference is mainly visible in the intercept. The intercept is inaccurate because the calculated grain size, 160 nm, differs from the assumed grain size, 100 nm. (This is also visible in the error of the intercept, which is larger than the value itself.) Using only a number of reflections, here the first 5 reflections, also has a large influence on the results obtained, namely the intercept is negative, Table 3.6. To solve this problem reflections of only one plane are used, for example the {111} and the {222} reflections. However, this may also generate a significant error simply because of bad statistics.

Table 3.6. Recalculated deformation strain and intercept assuming a grain size of 100 nm and a maximum micro stress of 3.5 GPa.

	Mechanical XEC	Anisotropic XEC	First 5 reflections
ε_{hh}	$8.9 \cdot 10^{-3} \pm 3 \cdot 10^{-5}$	$9.1 \cdot 10^{-3} \pm 2 \cdot 10^{-3}$	$1.1 \cdot 10^{-2} \pm 3 \cdot 10^{-3}$
Intercept [m^{-1}]	$1.0 \cdot 10^{7} \pm 4 \cdot 10^{5}$	$6.3 \cdot 10^{6} \pm 3 \cdot 10^{7}$	$-1.1 \cdot 10^{7} \pm 4 \cdot 10^{7}$

Conclusion

The lattice spacing measurements have confirmed the conclusions from the previous section, i.e. the macro stress is very high and the XEC are very anisotropic. Determining the grain size and the deformation strain in sputtered coatings is far from a straightforward procedure. The conclusions that may be drawn from the experiments are:

- It is impossible to determine accurately the grain size using the Williamson-Hall plots for these coatings.
- The deformation strain can be determined and is found to be very high and not directly related to the macro stress.

References

1 H.M. Gabriel and K.H. Kloos, Thin Solid Films 118 , 243 (1984).
2 Private communications with D. Tan of the Technical University of Eindhoven.
3 D.L. Smith, Thin Film Deposition: Principle & Practice, Mc Graw Hill, New York, 1995
4 J.A. Thorton, Ann. Rev. Mater. Sci. 7, 239 (1977).
5 C. Quaeyhaegens, G. Knuyt, J.D'Haen and L.M. Stals, Thin Solid Films 258, 170 (1995).
6 J. Pelleg, L.Z. Zevin S. Lungo and N. Croitoru, Thin Solid Films 169, 117 (1989).
7 U.C. Oh and Jung Ho Je, J. Appl. Phys. 74 (3), 1692 (1993).
8 R. M. Bradley, J.M.E. Harper and D.A. Smith, J. Appl. Phys. 60(12), 4160 (1986).
9 Lock See Yu, M.E. James, J.J. Cuomo and D.A. Smith, J. Vac. Sci. Technol. A 4(3), 443 (1986).
10 B. Rauschenbach and K. Helming, Nucl. Instrum. Methods. Phys. Res. B 42, 216 (1989).
11 J.W. Gerlach, U Preckwinkel, H. Wengenmair,T. Kraus and B. Rauschenbach, Appl. Phys. Lett. 68 (17), 2360 (1996).
12 G. Dreier, S. Schmauder, Scripta Metall. Mater. 28 (1993) 103.
13 F.M. D'Heurle, J.M.E. Harper, Thin Solid Films 171 (1989) 81.
14 C.A. Davis, Thin Solid Films 226 (1992) 30.
15 H. Windischmann, J. Appl. Phys. 62(5) (1987) 1800.
16 Y.S. Touloukian, R.K. Kirby, R.E. Taylor, T.Y.R. Lee, Thermophysical properties of matter, Nonmetallic Solids, Vol 13, IFI/Plenum, 1977, p1322.

17 Metals handbook, Vol 3, 9th ed., American Society For Metals, Ohio, USA, 1980 p. 441.
18 J.-D. Kamminga, Th.H. de Keijser, R. Delhez, E.J. Mittemeijer, Thin Solid Films 317 (1998) 169.
19 I.C. Noyan, J.B. Cohen, Residual stress, Springer-Verlag Inc., New York, 1987.
20 J.O. Kim, J.D. Achenbach, J. Appl. Phys. 72 (5) (1992) 1805.
21 H Dölle, J. Appl. Crystallogr. 12 (1979) 489.
22 J.G.M. Berkum, G.J.M. Sprong, Th.H. Keijzer, R. Delhez, E.J. Sonneveld, Powder Diffraction 10(2) (1995) 129.
23 S. Nagakura, T. Kusunoki, F. Kakimoto, Y. Hirotsu, J. Appl. Crystallogr. 8 (1975) 65.
24 F. Bollenrath, V.Hauk, E.H. Müller, Z. Metallkde. 58 (1967) 76.